



Cite this: *Nanoscale*, 2019, **11**, 932

Quantification of cellular associated graphene and induced surface receptor responses†

Zeid A. Nima, *^a Kieng Bao Vang, ^a Dmitry Nedosekin, ^b Ganesh Kannarpady, ^a Viney Saini,^a Shawn E. Bourdo, ^a Waqar Majeed,^a Fumiya Watanabe, ^a Emilie Darrigues, ^a Karrer M. Alghazali,^a Raad A. Alawajji,^a Dayton Petibone,^c Syed Ali,^d Alexandru R. Biris,^e Daniel Casciano,^a Anindya Ghosh,^a Gregory Salamo,^f Vladimir Zharov*^b and Alexandru S. Biris*^a

The use of graphene for biomedical and other applications involving humans is growing and shows practical promise. However, quantifying the graphitic nanomaterials that interact with cells and assessing any corresponding cellular response is extremely challenging. Here, we report an effective approach to quantify graphene interacting with single cells that utilizes combined multimodal-Raman and photoacoustic spectroscopy. This approach correlates the spectroscopic signature of graphene with the measurement of its mass using a quartz crystal microbalance resonator. Using this technique, we demonstrate single cell noninvasive quantification and multidimensional mapping of graphene with a detection limit of as low as 200 femtograms. Our investigation also revealed previously unseen graphene-induced changes in surface receptor expression in dendritic cells of the immune system. This tool integrates high-sensitivity real-time detection and monitoring of nanoscale materials inside single cells with the measurement of induced simultaneous biological cell responses, providing a powerful method to study the impact of nanomaterials on living systems and as a result, the toxicology of nanoscale materials.

Received 23rd August 2018,
Accepted 10th December 2018

DOI: 10.1039/c8nr06847j

rscl.li/nanoscale

Introduction

Due to its unique structure, chemistry, and surface functionality, graphene is currently one of the most intensely studied nanomaterials.^{1–3} It has potential uses in a range of applications, from nanoelectronics⁴ to composites⁵ to nanomedicine and biology.^{6–8} However, exposure to this nanomaterial also poses a significant risk to the environment^{9,10} and, potentially, to humans.^{11,12} In fact, graphene has a relatively complex and dynamic toxicity profile, most likely as a

result of its shape, size, number of layers, surface chemistry, and bioactivity.^{13,14} Its strong interaction with proteins and its unique pharmacokinetic profile¹⁵ lead to complicated behavior *in vitro* and *in vivo*. However, graphene's biodistribution and interactions with tissues and cells is not well understood. In addition, for any graphene toxicological studies, it is important to distinguish the exposure dose (amount of graphene introduced into the medium) from its effective dose (amount of graphene that actually interacts with the cells).

The detection and, particularly, the quantification of small amounts of graphene in biological systems is challenging due to its carbon-based composition,⁵ low fluorescence, and low microscopy imaging contrast. As a result, it is challenging to precisely quantify the amount of graphene in cells and tissues, making it difficult to adequately assess the effects of exposure to different doses of graphene. For example, analytical methods such as Inductively Coupled Plasma-Mass Spectrometry (ICP-MS) and fluorescence that work well for quantifying metal/metal oxide or semiconducting nanomaterials in tissues^{16–19} do not work for graphene, since they have limitations in distinguishing between the carbon structure of the nanomaterial and biological tissues. An interesting method for the quantification of bovine serum albumin (BSA) coated single-walled carbon nanotubes, based on their inherent NIR fluorescence, was presented recently, but this

^aCenter for Integrative Nanotechnology Sciences, University of Arkansas at Little Rock, 2801 S. University Ave., Little Rock, AR 72204, USA. E-mail: zanima@ualr.edu, asbiris@ualr.edu

^bArkansas Nanomedicine Center, University of Arkansas for Medical Sciences, 4301W. Markham St, Little Rock, Arkansas 72205, USA. E-mail: zharovvladimirp@uams.edu

^cDivision of Genetic and Molecular Toxicology, National Center for Toxicological Research, Jefferson, AR 72079, USA

^dDivision of Neurotoxicology, National Center for Toxicological Research, Jefferson, AR 72079, USA

^eNational Institute for Research and Development of Isotopic and Molecular Technologies, 67-103 Donat Street, RO-400293 Cluj-Napoca, Romania

^fInstitute for Nanoscience and Engineering, University of Arkansas at Fayetteville, AR 72701, USA

†Electronic supplementary information (ESI) available. See DOI: 10.1039/c8nr06847j

approach might not be applicable for graphene-type materials.²⁰ Thermogravimetric analysis has been proposed to quantify graphene,⁶ but its limited sensitivity might not allow detection at the expected picogram levels of intracellular graphene. In summary, a technique to quantify and analyze the toxicological risk of graphene to humans is needed. Therefore, new approaches that assess graphene's impact at the cellular and molecular level are required in order to quantify the exposure dose resulting in the development of risk/benefit models.^{21,22}

Methods

Graphene treatment

Approximately 3 g of graphene flakes (1–1.2 nm thick, Angstrom Materials, product number: N002-PDR) were placed in a 2 L flask, then 300 mL of ultra-high purity 18 M Ω deionized (DI) water were added. Next, 600 mL of concentrated H₂SO₄ (Sulfuric Acid Certified ACS Plus, 95.0 to 98.0%, Fisher chemical) and 200 mL of concentrated HNO₃ (Nitric Acid Certified ACS Plus, 70%, Fisher chemical) were carefully introduced to the graphene–water mixture and stirred (using a Teflon-coated magnetic stir bar) for two days. Prior to filtration, aliquots (~250 mL) of the reaction mixture were diluted by 50% (v/v) with 18 M Ω DI water two times sequentially in order to lower the acid concentration during the filtration steps. The resulting mixture was then introduced into a vacuum filtration setup (47 mm diameter fritted glass equipped with a Millipore 0.2 μ m GTTP Isopore membrane filter) and allowed to filter. The resulting mixture was then added, and the remaining solids were washed successively with 18 M Ω DI water until the pH of the filtrate was similar to that of the water. The final powdered sample was then collected into a glass container and allowed to dry in a convection oven at a temperature of 60–80 °C.¹⁴

Graphene dispersion

20 mg of functionalized graphene were dispersed in 200 mL of ultra-high purity DI water by bath sonication for 6 hours. Next, the dispersion was centrifuged at 3200 rpm and the supernatant was decanted, leaving the sediment at the bottom of the centrifuge tube. After decanting, the supernatant was again sonicated for 3 hours before fabrication of graphene films.

Graphene film fabrication

A small amount of the graphene dispersion was filtered through an alumina membrane (Whatman Anodisc 25 CAT No. 6809-6022). As the water filtered through the membrane, it left a thin, uniform film of graphene on top of the alumina membrane. After air drying, the alumina membrane was dissolved in 3 M of NaOH. The floating graphene film was rinsed with multiple applications of ultra-high purity DI water to remove any traces of NaOH. The graphene film was then lifted onto a silicon substrate, glass slide, and quartz crystal simultaneously to obtain similar film thickness on all the substrates. Next, the graphene film was dried on a hot plate

(90 °C). As the water evaporated, the graphene film came in contact with the silicon substrate, glass slide, and quartz crystal and adheres to the substrate after completely drying. Any wetting of the film after this step does not remove graphene from its substrate. The graphene film fabrication step was repeated with different volumes of graphene dispersion in order to generate samples with varying graphene film thicknesses. The graphene film on the silicon substrate was used for Raman spectrum and AFM (Atomic Force Microscopy); films on glass slides were used for PAM (Photoacoustic Microscopy) studies; and the quartz crystal was used to determine the weight of the films.

QCM standard curve

A series of graphene thin films (22 mm diameter) with different thicknesses were prepared, as presented before. Mass for each square sample was determined by using a quartz crystal microbalance (QCM). The films were lifted off simultaneously onto 6 MHz gold-coated quartz crystals (1.4 cm diameter), glass slides (2.5 cm \times 7.5 cm), and silicon substrates (approximately 5 mm \times 5 mm). The oscillation frequency of the quartz crystals before and after graphene film deposition was measured. The difference between the frequencies was used to determine the weight of the graphene film. Special care was given to measure the mass of dried graphene after any moisture adsorbed on its surface was removed. AFM was employed to measure the thickness of graphene films on the quartz and silicon substrates at several places. Although the films were not perfectly smooth, having RMS nanoscale roughness, they were rather uniform for both the quartz crystals and silicon substrates. Similarly, a 1-micron area was scanned with Raman spectroscopy at several places on the quartz crystals and silicon substrates; the results confirmed that the films were uniform. This indicates that the weight of a given area of graphene film with a specific concentration of graphene on both the quartz crystals and silicon substrates was identical throughout the entire film.

Raman and PAM

After determining the mass, we scanned each square with a 785 nm laser using a Raman spectrometer in a DuoScan® mode. D-bands position and intensity values were recorded for each sample within a 10 \times 10 μ m spot size, and then the area under curve was calculated using LapoSpec® software. After acquiring the Raman signal and corresponding mass (weight), we constructed a standard curve (Fig. 1); the measurements were repeated four times. To calibrate for the PAM analysis, another set of 12 graphene thin films was prepared on 1 mm-thick glass slides (non-transparent silicon substrate is not compatible with PAM). The central part of each graphene film was transferred to the silica substrate and weighed by QCM. The remaining part of the graphene film was analyzed by PAM images of 100 \times 100 μ m areas of three different sides of each sample. For each image, a random set of regions of interest (ROIs) was selected and the PA signal was integrated throughout each ROI. Similar to Raman microscopy, the calibration graph was constructed using the integrated PA signal vs. graphene weight.

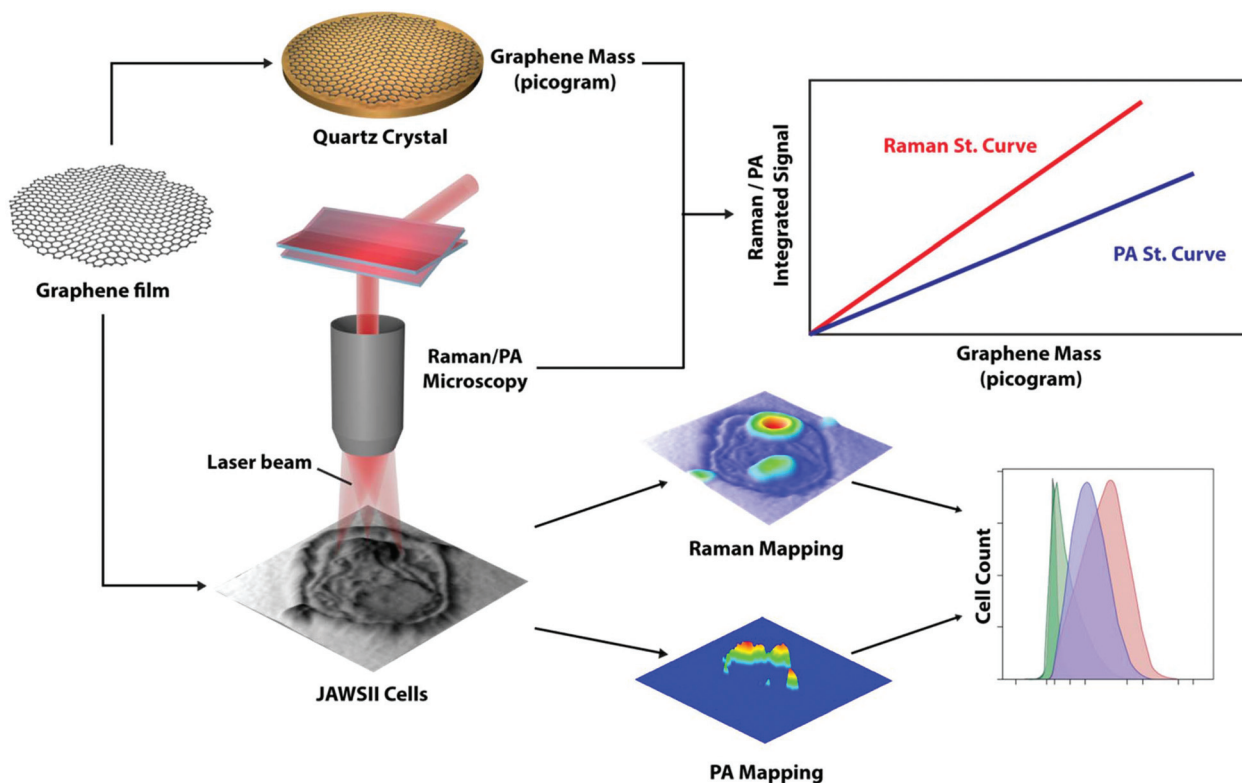


Fig. 1 Multimodal Raman-PA graphene quantification strategy for analyzing a nanomaterial's impact on cellular morphology and function. The quantitative graphene uptake data provided by label-free Raman and PA imaging are correlated to changes in expression of surface markers on the DCs. Raman and PA calibration was performed by analyzing graphene reference material of known density.

Cell systems

The JAWSII cells were a bone marrow-derived immortalized cell line from p53^{-/-} C57BL/6 mice (American Type Culture Collection (ATCC), CRL-11904). They were grown in 10% fetal bovine serum (FBS) (ATCC, 30-2020) and Alpha Minimum Essential Medium (Corning, Cat. 10-022-CV), 1% penicillin + streptomycin, and 5 ng mL⁻¹ murine GM-CSF (R&D Systems, 415-ML-050, Minneapolis, Minnesota). The PC12 cells were pheochromocytoma cells derived from the rat adrenal gland (ATCC, CRL-1721). They were cultured in 10% heat-inactivated horse serum (ATCC, 30-2041), 5% FBS (ATCC), 1% penicillin + streptomycin, and RPMI-1640 Medium (ATCC, 30-2001). The breast cancer cell line (MDA-MB-231, ATCC HTB-26) was a human-derived adenocarcinoma from mammary gland/breast tissue. These cells were cultured in 10% FBS (ATCC), 1% penicillin + streptomycin, and DMEM (ATCC, 30-2002). JAWSII, MDA-231, and PC12 cells were maintained in an incubator at 37 °C and 5% CO₂.

Quantification of graphene content per cell

Three cell lines, JAWSII, PC12, and MDA-231 were used as models for the quantification of graphene accumulation at different time points (0, 2, 4, 6, and 24 h). Each cell line was plated in four chamber slides (Sigma); each chamber contained a silicon wafer (25 mm × 15 mm). 10 × 10⁴ cells per chamber were plated for 24 hours; at each time point, cells were treated with the same medium containing different gra-

phene concentrations (0, 1, 5, 10, and 50 µg mL⁻¹). After each time completion, cells were fixed and washed multiple times with 1× PBS then multiple times with DI water to remove any graphene residue. The fixed cells were then air-dried and stored at -20 °C prior to Raman quantification. For PA analysis, JAWSII cells were incubated with graphene (0, 1, 5, 10, and 50 µg mL⁻¹ of graphene and 0, 2, 4, 6, and 24 h incubation times) in a two-chamber slide (Sigma) directly on the glass surface. The level of PA background signal was estimated for control cells and used to normalize all the PA data. For each sample, 14 PA and optical microscopy images were acquired (3–20 cells per image, individual cells were preferred over clusters, cells with extra-large clusters of graphene were removed from analysis) with a total of 60–80 cells per sample. Optical and PA images were analyzed using a custom ImageJ macro, allowing manual selection of ROIs based on cell boundaries and automatic integration of corresponding PA signal over each ROI. For both Raman and PA analyses, multiple series of independent experiments were conducted, and in each experiment a random approach of selecting cells for scanning was followed.

Raman quantification

Each sample (time point and concentration) for each cell line (JAWSII, PC12, and MDA-231) was treated in the same way. Chamber slides were transferred to the Raman instrument to perform Raman measurements. A Raman spectrometer

(Horiba Jobin Yvon LabRam HR800, Edison, New Jersey) that assembled with a diode laser (784 nm as well as 514 and 633 nm excitations) on an Olympus BX-51 microscope platform with a 100 \times micro-objective. The spectra were collected using DuoScan[®] mode, *i.e.* averaging mode (In this mode the laser is continuously scanned over a user-defined square surface) with the 600 line per mm gratings at an identical acquisition time (20 s). Spectra were baselined and background-corrected, then replotted using OriginLab software. The spectrometer was connected to a three-dimensional (x - y - z) automatic adjustable stage with spatial resolution of 1 μ m. For all measurements, the Raman spectrometer was calibrated using the substrate's Si-Si Raman spectral signature at the 521 cm^{-1} Raman shift.

Laser scanning PA microscope

The custom built laser scanning PA microscope used in this study was based on an Olympus IX81 inverted microscope platform and operated in optical resolution mode with the laser beam spot much smaller than the acoustic resolution of the ultrasound detection system. XY galvo mirrors (GVSM002, Thorlabs Inc., Newton, NJ) steered a 532 nm laser beam (LUCE 532, Bright Solutions, Italy) coupled to the microscope *via* a single mode optical fiber. The laser beam was then exposed to the sample from the bottom through a 10 \times objective (DPlan 10 \times , Olympus Inc.). Acoustic waves were then collected by a focused transducer (V316, 20 MHz, 12 mm focal distance, Olympus-NDT Inc.) mounted over the sample (transmission configuration). To ensure acoustic coupling between the cells on a glass slide and the transducer, a plastic custom cup (fabricated out of a $\frac{3}{4}$ inch disposable weighing dish) was mounted to the glass slide by using epoxy glue and was filled with DI water. The resulting signals that were generated by the transducer were then further amplified by a 20 dB amplifier (0.05–100 MHz bandwidth, AH-2010-100, Onda Corp.) and collected and recorded by a computer equipped with a high-speed digitizer (PCI-5124, 12-bit card, 128 MB of memory, National Instruments, Austin, TX). Both the system synchronization as well as the laser triggering processes were performed by a digital waveform generator (DG4062, Rigol, Beijing, China). Laser beam spot size was estimated to be \sim 2.3 μ m (FWHM), and laser step scan was around 2 μ m. For each sample point, 40 PA signals were averaged and the maximal amplitude values of the acoustic waves were collected and recorded. Optical digital microscopic images were also collected by using a DP72 camera (Olympus Inc) that was fitted with a custom ring illuminator installed on the transducer.⁴⁷

PA imaging in high-resolution mode (optical resolution PA microscopy) was performed on the same setup using a 100 \times Plan Fluor focusing objective, providing lateral as well as axial imaging resolution of 300 and 900 nm, respectively. Multiple 2D PA and fluorescence images were acquired along the vertical microscope axis by displacing the focusing objective with a 500 nm step. Cells were stained with FITC (membrane) and DAPI (nuclei) to help us identify whether graphene is membrane bound or actually penetrates into cells. 3D reconstruction of graphene absorption and fluorescence distribution was

performed using ImageJ software. Maximal laser energy in high-resolution PA imaging was 1 nJ per pulse. The resolution of PA imaging was determined based on the diameter of excitation laser beam (more information in ESI section[†]). The presented quantification data was acquired with beam diameter of 2.3 μ m. High-resolution PA imaging mode was performed with smaller excitation beam (approximately 295 nm) providing lateral and axial imaging resolution of \sim 300 nm and \sim 900 nm. This allows 3D analysis of graphene distribution within a single cell at a sub-cellular level.

Flow cytometry

JAWSII DCs were treated with the following concentrations of graphene: medium alone, 1, 5, 10, and 50 $\mu\text{g mL}^{-1}$ for 2, 3, 24, and 72 hours. Afterwards, cells were washed and 1.0×10^6 cells were stained and incubated at 4 $^{\circ}\text{C}$ for 30 minutes with the following antibodies (Affymetrix, eBiosciences): CD11c (N418), CD86 (GL1), CD80 (16-10A1), MHC Class I (3 4-1-2S), CD40 (IC10), MHC Class II (M5/114/15/2), and CD205 (205yekta). Subsequently, cells were thoroughly washed and flow cytometry was performed using an LSRFortessa instrument (BD Biosciences, Franklin Lakes, NJ) at the Flow Cytometry Core Facility at the University of Arkansas for Medical Sciences (Little Rock, AR). The data were analyzed by using the FlowJo software package (TreeStar, Ashland, OR).

Annexin V

Apoptosis was analyzed and detected using an Annexin V Apoptosis Detection kit (eBioscience). Cells were treated with medium alone, 1, 5, 10, and 50 $\mu\text{g mL}^{-1}$ of graphene for 2, 4, 6, and 30 hours. Next, 1.0×10^6 cells were washed with 1 \times binding buffer and stained with 5 μL of fluorochrome-conjugated Annexin V. After 15 minutes of incubation at room temperature, cells were thoroughly washed and then resuspended and propidium iodide was carefully added according to recommendations of the manufacturer.

Transmission electron microscopy

1×10^6 JAWSII cells were seeded in 35 mm dishes one day prior to graphene exposure. 1 $\mu\text{g mL}^{-1}$ graphene was added to cells, which were then incubated for 24 hours before fixation. Samples were then prepared based on the experimental procedure described by Cocchiari *et al.* (2008)⁴⁸ with some minor modifications. Cells were fixed for 20 minutes on ice with 2.5% glutaraldehyde in 0.1 M sodium cacodylate buffer. Subsequently, cells were washed several times for 5 minutes each time with 0.1 M sodium cacodylate buffer. Cells were post-fixed for 1 hour at room temperature in the dark with 1% osmium tetroxide and 0.8% potassium ferricyanide in 0.1 M sodium cacodylate buffer. Samples were washed with 0.1 M sodium cacodylate buffer a few times for 5 minutes and stained with 1% tannic acid for 20 minutes on ice then for 1 hour with 0.5% uranyl acetate at room temperature. Next, the samples were carefully dehydrated by using a graded ethanol and then embedded into epoxy resin. Thin sections (70 nm) were carefully cut by using a diamond knife on a Leica

UltraCut7-UCT microtome and post-stained with 1% uranyl acetate as well as Reynold's lead citrate (Electron Microscopy Sciences) before analysis and viewing. TEM images of JAWS cells were collected by JEOL JEM-2100F at 80 kV.

Results and discussion

Combinatorial Raman-photoacoustic quantification method

We have developed a novel combinatorial methodology based on the unique, highly sensitive Raman and photoacoustic (PA) spectroscopic signatures of graphene. Raman spectroscopy, an inelastic light-scattering process, takes advantage of the differences in energy between the scattered photons and the excitation incident photons. Graphene is a light scattering material due to its unique hexagonal ring structure, which has six phonon dispersion bands—three acoustic (A) and three optical (O) modes.⁸ Two of these modes are energetically degenerated and Raman active.^{7,13} Based on these properties, we used graphene's strong Raman D-band ($1300\text{--}1400\text{ cm}^{-1}$) as the unique signature to detect the materials' distribution and interaction with cells. PA microscopy (PAM), is based on the thermoelastic expansion of a sample when it absorbs light. The acoustic waves caused by this expansion are detected using ultrasound transducers, and the magnitude of the acoustic wave is proportional to the absorbed laser energy.²² PAM can be used with light-scattering samples, such as live cells and thick tissue sections, because elastic scattering produces no thermoelastic expansion. Generally, biological tissues have low attenuation for ultrasound waves with frequencies below 50–100 MHz. For example, the soft tissue attenuation coefficient [dB cm^{-1}] is around 0.9ν , where ν is the frequency in MHz.²³ As a result, PAM is suitable for high-speed imaging with nano-second laser excitation and has been utilized to detect carbon nanotubes in flow at velocities up to 2.5 m s^{-1} ;²¹ PA *in vivo* flow cytometry has also been used to analyze graphene pharmacokinetics in blood.²⁴ Moreover, graphene has a very high light absorbance, with each atom-thick layer absorbing $\sim 2.3\%$ of incident light in the visible and near-infrared spectral ranges.²⁵

Impact of graphene in dendritic cells

One of the most important aspects of graphene's use in biological organisms is its biodistribution. Recently, Chen *et al.*²⁶ showed that the primary targets of carbon nanomaterials are the kidney and spleen, with the greatest concentration being found in the marginal zones of the spleen—precisely where dendritic cells (DCs) accumulate.²⁶ If a critical loss of DC function occurs, a multitude of immune dysfunctions such as autoimmunity, chronic inflammation, and allergies could result.^{27,28} In the resting state, DCs are immature until they encounter a foreign signal, which leads to their maturation and the initiation of an immune response.²⁷ Pattern recognition receptors on the surface of DCs can recognize a host of signals, such as microbes, foreign proteins, lipids, nucleic acids, and carbohydrates. Once these danger signals are recognized, DCs have a unique ability to endocytose, process, and load them onto

major histocompatibility markers (MHC) for presentation to naïve T cells.^{27,28} The markers CD11c (integrin alpha X) as well as DEC-205 (a type I cell surface protein also known as CD205) are known to be expressed by lymphoid dendritic cells.²⁹

Compared with other cells of the immune and non-immune system, DCs are uniquely poised to uptake particles to induce T cell activation, expansion, and function, making it crucial to evaluate the impact of graphene on DCs. To do so, we chose JAWSII cells, a bone marrow-derived, immortalized mouse DC cell line that is commonly used in functional immunology studies to model primary DCs *in situ*. The presence or absence of a receptor can indicate the state of readiness of an immune cell.^{27,28,30–32} Higher or lower expression of a receptor on an immune cell indicates the cell's state of activation or inactivation and, as a result, its potential for mobilizing an innate or adaptive immune response. JAWSII DCs have all the hallmarks of an immature DC, expressing low surface receptor markers such as MHC class I, MHC class II, and costimulatory markers known to be important in T cell activation and stimulation: CD80, CD86, and CD40.^{30–32} Here, we present an approach to detect and quantify, down to the level of a single cell, the amount of graphene interacting with JAWSII cells and demonstrate the impact that graphene exposure has on JAWSII cell surface receptor expression levels.^{29,31,32}

Raman and photoacoustic spectroscopic signature of graphene

Our technique for graphene quantification, shown in Fig. 1, begins with a correlation between the integrated spectral graphene signature (Raman and PA) and the mass of the nanomaterial in the analyzed cellular area. This provides distribution data about the nanomaterial that is internalized or attached to the cell membrane. By establishing this correlation, we then measure and quantify the spectroscopic signals collected from individual cells (Fig. 1). Our goal was to take advantage of the strong laser scattering and absorption by graphene, using Raman and PA spectroscopy independently to measure and analyze the amount of graphene per single cell, then determining the degree of similarity in the corresponding experimental measurements. Both methods were able to determine relatively same trends for the amount of graphene that interacts with the various cellular samples, despite of the heterogeneity of the samples and the fundamental physical base that each technique. In this study we have used a 785 nm laser excitation to acquired Raman signal. Given the ability of this type of laser to have a relatively deep tissue penetration, we believe that in the future, this method can be potentially applied to thin tissue and multilayer cells. However, in our current study we have applied PA and Raman methods on a 2D monolayer cells only. We did not explore tissue or cellular multilayer approach yet. The proposed graphene quantification approach utilizes excitation lasers with beam diameter much smaller than cell size ($2.3\text{ }\mu\text{m}$ for PA mode and $1\text{ }\mu\text{m}$ for Raman mode). The total signal from the aggregate/flake is a integration of the PA/Raman signal collected within the 2D raster scan ($10\text{ }\mu\text{m} \times 10\text{ }\mu\text{m}$ for Raman) (Fig. 1). In general, 2D raster scanning (DuoScan®, averaging mode) sends laser

energy into different areas of the sample and acquires signals from each location independently.

Graphene mass determination

The weights of graphene samples with varying masses were measured by QCM, a technique first reported by Sauerbrey in 1959.³³ Often used to quantify biomedical molecules,^{34–39} QCM is based on the change in the mass of the quartz crystal relating to a change in crystal oscillating frequency, as follows:

$$\Delta f = -C_f \times \Delta m \quad (1)$$

where Δf is the change in frequency, Δm is the change in mass, and C_f is the sensitivity factor of the crystal, which is 81 Hz μg^{-1} cm² (6 MHz crystals) at room temperature for AT-cut quartz crystals.

Depositing the graphene samples directly on the QCM, we calibrated their Raman/PA signals based on sample weight. The Raman/PA signals from the graphene samples in the cells were then found, and calibration curves plotted the intensity of the signals collected over select areas of the samples *versus* the graphene mass calculated for the same areas. As a result, we were able to use this approach to determine graphene within individual cells when compared to cells without graphene.

Visualization of graphene interaction with individual cells

The graphene used in this study was slightly oxidized for relative facile processing (X-ray photoelectron spectroscopy (XPS) analysis and FTIR, ESI, Fig. S1–S3†). We characterized the morphology of 0.5–3.5 nm thick graphene samples (post treatment) (ESI Fig. S4†) using atomic force microscopy (AFM), transmission electron microscopy (TEM), and scanning electron microscopy (SEM). Scanning and transmission electron microscopy did not provide the correct size distribution of the graphene flakes because these techniques were found to be generally unable to accurately distinguish between individual or overlapped flakes. Therefore, AFM was used to find the lateral size distribution of our sample after the final processing (oxidation, sonication and centrifugation) (ESI Fig. S4(B)†). XPS indicated that the major elements present were C, O, and S, while FTIR indicated the presence of several oxygen-rich functionalities on the samples' surfaces (ESI Fig. S1–S3†). The crystallite size (L_a) of graphene flakes was calculated to be 21.7 nm based on Cancado's equation.^{40,41} Graphene's stability (as measured by optical absorption UV-Vis-NIR) in the JAWSII and PC12 media over 24 hours was found to be excellent, particularly for the 1 $\mu\text{g ml}^{-1}$ concentration (ESI Fig. S14 and 15†). However, the higher concentration of 50 $\mu\text{g ml}^{-1}$ showed a small level (less than 10%) of sedimentation. Stability of graphene in various cellular media is critical, since a high degree of bottom sedimentation could result in a lower available concentration of graphene in the solution to interact with the cells. In our case, once exposed to the graphene media, the cells were observed to present strong interactions with the graphene. Combined AFM and TEM analysis clearly indicated the ability of graphene to interact with and be inter-

nalized by the JAWSII cells (Fig. 2) but could not accurately quantify intracellular graphene. However, Raman and PAM enabled quantification of the associated (internal and/or membrane associated) graphene in JAWSII cells using high-resolution data on the volume distribution of graphene inside the cells (ESI Fig. S10, Videos S1 and S2†), although the resolution of both Raman and PAM could be possibly hindered by light diffraction and some possible nonlinear phenomena being present for large, bulky samples.^{42–44}

Raman (D-band) integrated intensity and/or PA signals from the films integrated over 10 $\mu\text{m} \times 10 \mu\text{m}$ areas were compared to the mass of graphene calculated using graphene density ($\text{pg } \mu\text{m}^{-2}$), as measured by QCM. Linear calibration curves were acquired for Raman (30 random similar sized areas) and PAM (Fig. 3(a and e)). Fig. 3(b–d) and (f–h) shows optical images of JAWSII cells exposed to graphene, demonstrating the ability of Raman and PAM to provide 2D mapping of graphene's interactions with single cells. Fig. 3(i) shows the 2D Z-stacked Raman mapping of a JAWSII cell exposed to graphene, which is in excellent correlation with the earlier studies presented by Holt *et al.*²⁰ that investigated interactions of cells with single-walled carbon nanotubes. Fig. 3(j) shows the 3D high resolution PA and fluorescence microscopy visualization of the graphene interaction with a single JAWSII cell incubated with 1 $\mu\text{g mL}^{-1}$ of graphene for 4 hours. The analysis was done by collecting 2D planar images and which were reconstructed into a 3D architecture. The establishment of linear relationships between graphene mass and spectroscopic signal therefore allowed for quantification of graphene mass per cell at around 200 fg sensitivity (see ESI† for more details).

Quantification of graphene's interactions with single cells

Generally, Raman and PA techniques provided the quantification of total associated graphene inside the cells and/or the membranes without being able to differentiate between the graphene internalized or present within or on top of the cellular membrane. Additionally, we observed large variations in the amount of graphene/cell for each individual treatment condition. Despite of that limitation, we found, clear correlations/trends between the amount of graphene interacting with the JAWSII cells and both the graphene concentrations in the solution and the exposure times. The increase in interaction was found to be statistically significant at each treatment condition and time point (Fig. 4(a–c)). The results of the Raman analysis were further validated by using PAM to analyze cells incubated under identical graphene exposure conditions (Fig. 4(d) and (e), ESI Fig. S8 and S9†). Since there is no standard technique to validate Raman and PA quantification of graphene in single cells, we performed cross-correlation of Raman/PA data for the samples incubated under identical conditions, assuming identical uptake. Fig. 4(f) combines the data points from Fig. 4(a) and (d) and represents each concentration/incubation time combination as a single point. Overall, the PA and Raman data were relatively comparable, with a slightly higher absolute mass of graphene found by PA. However, this data should be seen more as a trend rather than an immediate precise corre-

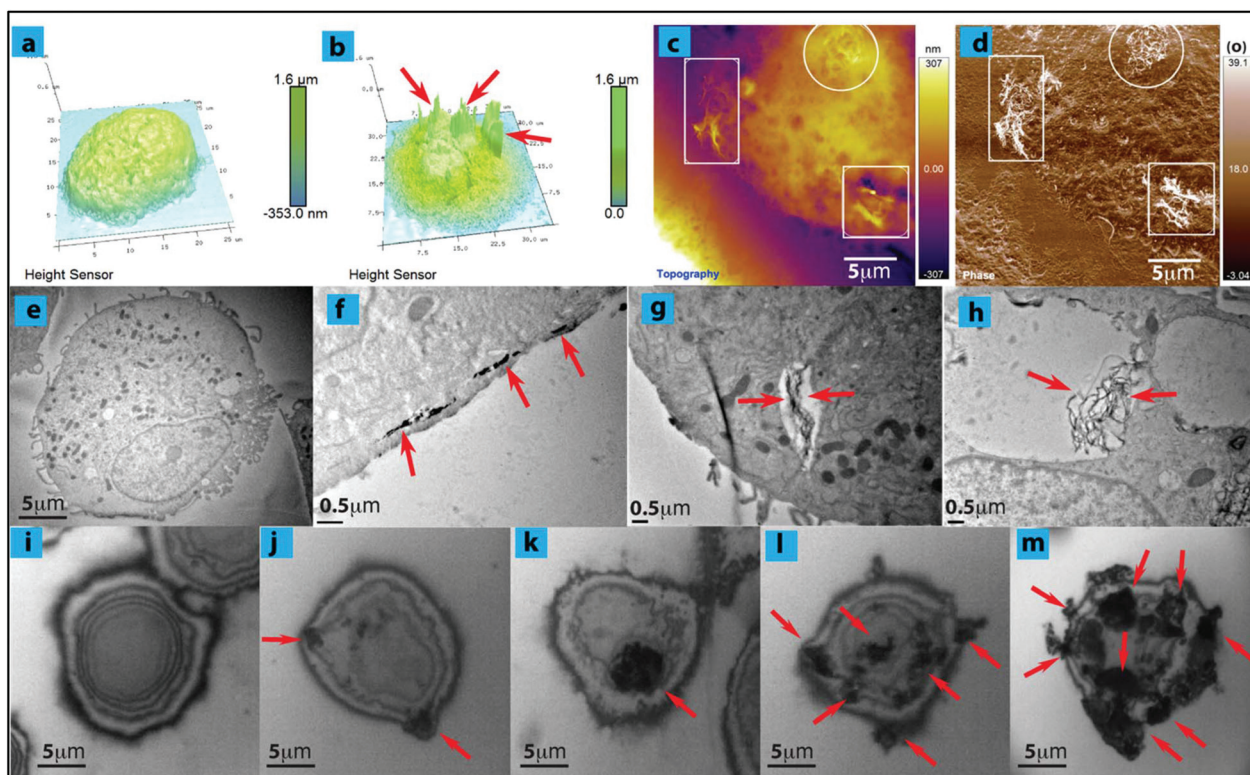


Fig. 2 Microscopic analysis of graphene samples used in this study and JAWSII cells after exposure to various concentrations of graphene. (a) AFM image of JAWSII cell without graphene (control); (b–d) AFM images of JAWSII cell with graphene that show the presence of the nanomaterial on the membrane of the cell (marked areas). (e–h) TEM images of the JAWSII cells incubated with graphene. The red arrows point to the graphene flakes on the surface of the cells. (e) control; (f–h) cells incubated with $1 \mu\text{g mL}^{-1}$ graphene for 24 hours show various cells exposed to graphene. (i–m) bright-field optical microscope images of cells. The red arrows point to the graphene flakes; (i) JAWSII control cell; (n–q) JAWSII cells incubated for 2 hours with $1, 5, 10,$ and $50 \mu\text{g mL}^{-1}$ of graphene solution, respectively.

lation. We believe that the differences in quantification values can be clearly understood through the experimental variations that include the heterogeneity of the cellular samples, differences in cell samples being seeded on various substrates (glass slide vs. silicon wafer for PA and Raman, respectively), cell selection procedures, as well as the variable fundamental detection mechanisms between Raman and PA. For comparison, we decided to study the interaction of graphene with additional cell lines originating from different tissues: breast cancer MDA-123 (used intensively as a model for breast cancer research) and PC12 (a pheochromocytoma cell derived from the adrenal medulla; useful for neuronal studies). JAWSII DCs were found to generally uptake significantly larger amounts of graphene compared to the PC12 and MDA231 cell lines (Fig. 4(a–c)). The uptake was also found to be impacted by time of exposure and graphene concentration in solution. The statistical analysis between the various time/concentration points for these cells is presented in ESI Fig. S20 and S21.† This uptake difference could possibly be attributed to the phagocytic nature of JAWSII cells vs. the non-phagocytic PC12/MDA-231 cells.

This result, while not surprising, confirms the need to quantify the effective dose, because different cell types derived from different organs can be expected to have different responses to

graphene exposure. Indeed, as shown by TEM, the treatment of JAWSII with $1 \mu\text{g mL}^{-1}$ of graphene for 24 hours resulted in efficient internalization of graphene (Fig. 2(e–h), 4(a–c), ESI Fig. S11 and S12†). Optical and electron microscopic analyses (Fig. 2(e–h) and (i–m)) indicated that a portion of the measured graphene resistant to several sample washings could still be attached to the cell surface membrane.

Most of the literature on graphene toxicity and efficacy studies indicates that observed responses result from the graphene exposure dose rather than the amount of graphene interacting with the cells (effective dose).^{45,46} To highlight this concept, we determined the distribution of graphene mass among JAWSII cells with various exposure times and graphene concentrations. PA spectroscopy was used to calculate the number of cells whose graphene uptake exceeded 0.3 or 2.5 pg (Fig. 5). These data demonstrated that the majority of cells acquired graphene (mass exceeding 0.3 pg or 150% of the PAM limit of detection). However, further accumulation of graphene depended primarily on graphene concentration and partially on exposure time. For example, accumulation of 2.5 pg of graphene in 40% of cells treated with $5 \mu\text{g mL}^{-1}$ graphene solution was achieved in 2 hours, while those treated with $1 \mu\text{g mL}^{-1}$ took almost 24 hours to reach a similar amount of

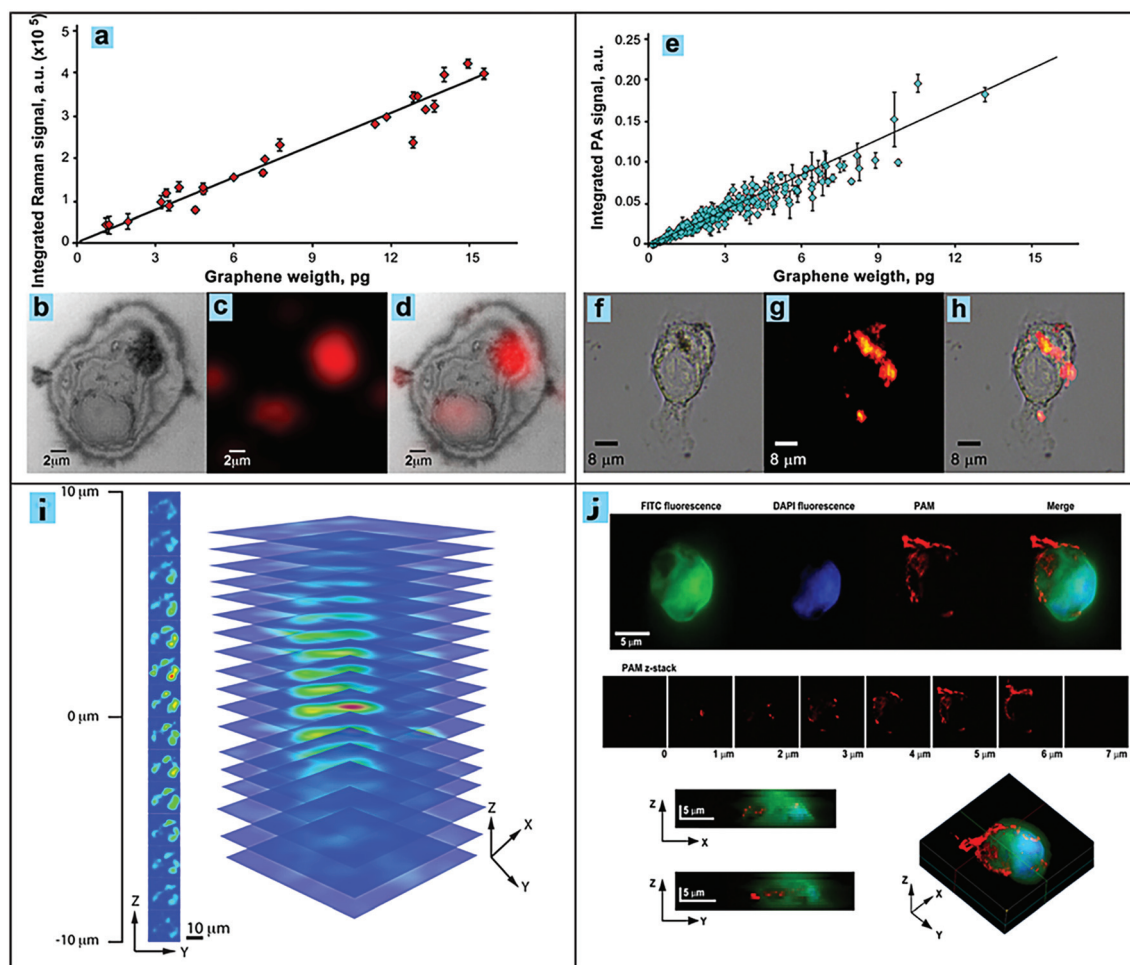


Fig. 3 Raman (a–d, i) and PA (e–h, j) spectroscopy analysis of the graphene interaction with single cells. Calibration of Raman and PA measuring systems with graphene reference materials shows a linear correlation between (a) integrated Raman ($R^2 = 0.95453$) or (e) PA ($R^2 = 0.967$) signals and the total mass of graphene (pg) over the analyzed intracellular area. Typical Raman imaging data for JAWSII cells exposed to $5 \mu\text{g mL}^{-1}$ of graphene for 4 hours: (b) bright-field cell image, (c) Raman signal 2D map, and (d) overlaid image. Typical PA imaging data: (f) bright-field cell image, (g) PA signal 2D map, and (h) overlay image. (i) z-Axis Raman mapping scan, step size was $1 \mu\text{m}$ in z-direction starting from -10 to $10 \mu\text{m}$. (j) (a) Visualization of the internalization of graphene by JAWSII cells via high resolution PA and fluorescence microscopy: individual fluorescence and PAM images of a single JAWSII cell incubated with $1 \mu\text{g mL}^{-1}$ of graphene for 4 hours; (b) full z-stack of PAM images for the cell; (c) 3D reconstruction of cell absorption by ImageJ.

graphene accumulation. In contrast, almost 100% of JAWSII cells treated with $50 \mu\text{g mL}^{-1}$ for 24 hours contained more than 2.5 pg of graphene per cell.

The quantity of intracellular graphene per cell and its effects on cellular physiological responses have not yet been thoroughly quantified in the literature. Specifically, the amount of graphene/cell that can cause a change in cell surface receptors on DCs is undocumented. DCs express several cell surface receptors that are upregulated when they come in contact with a “foreign signal,” resulting in their activation and maturation, which can lead to an immune response. This activation and maturation state is first characterized by an ability to increase the expression of the cell surface receptors: MHC class I, MHC class II, DEC-205, CD80, CD86, and CD40.^{30–32} The markers CD11c (integrin alpha X) and DEC-205 (a type I cell surface protein also known as

CD205) are expressed by lymphoid DCs. Once these receptors are upregulated on the DC cell surface, an immune response can ensue.

Having demonstrated the ability of our method to determine the amount of intracellular graphene per cell, we investigated the effective dose of graphene on DC physiology by evaluating the seven surface expression markers known to be involved in DC activation and maturation. We focused on two of these cell surface markers: the co-stimulatory molecule CD86, known to be involved in T cell activation, and MHC-I, known to present antigens to T cells. The cells were exposed to $1, 5, 10,$ and $50 \mu\text{g mL}^{-1}$ of graphene for 2, 24, and 72 hours (Fig. 6 and Fig. S16, S17, and S18†). The color of the histograms represents the overall expression of the surface receptors on the surface of the cell. We used shading to highlight the histograms of the negative staining control and the media

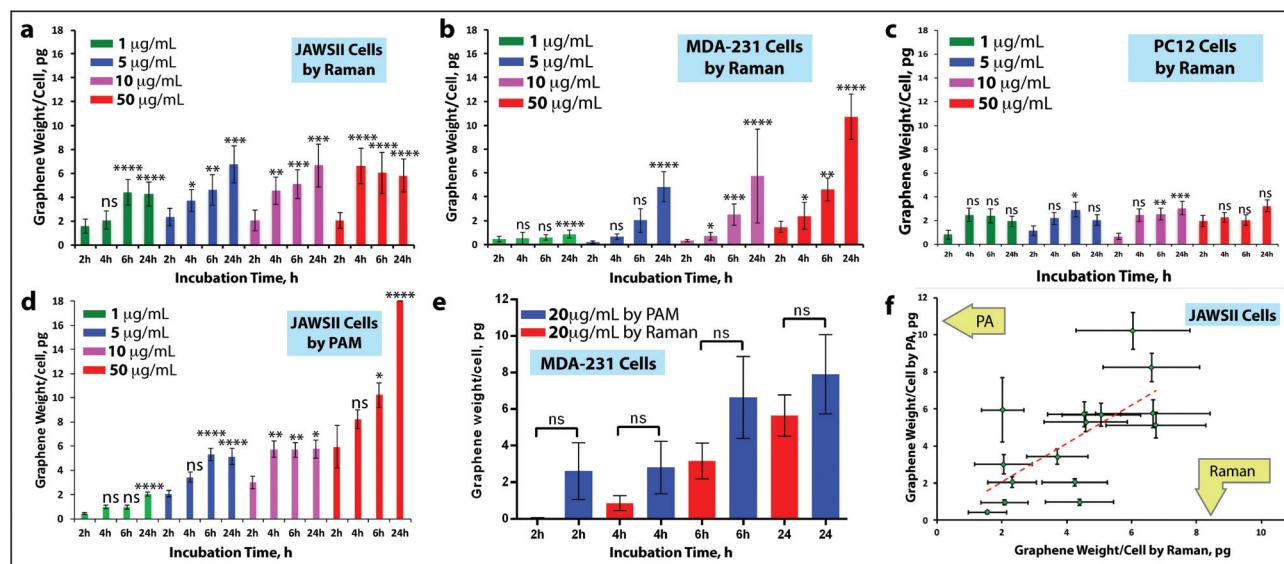


Fig. 4 Quantity of graphene taken in by JAWSII DCs is concentration and time dependent. Raman analysis of (a) JAWSII, (b) MDA-231, and (c) PC12 cells. (d) PAM analysis of JAWSII cells and (e) Raman analysis (red) and PAM analysis (blue) of MDA-231 cells. (f) cross-correlation between Raman and PA data for samples incubated under identical conditions. Red dash line represents an ideal (1 : 1) correlation between methods. Data are representative of 3 Raman and 2 PAM independent experiments; error bars are mean \pm standard error of the mean. Ordinary one-way ANOVA statistical analysis was conducted, ns: non-significant, $P < 0.05$, confidence limits CL = 95%.

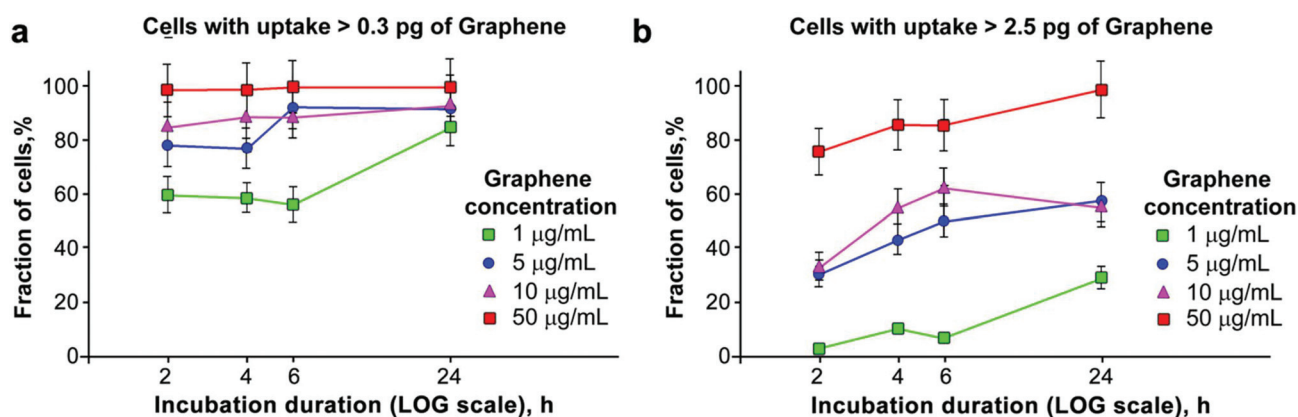


Fig. 5 PA data shows an increase in the number of cells with large graphene content over time (accumulation dynamics). Relative fraction of JAWSII cells with graphene content exceeding (a) 0.3 and (b) 2.5 pg was calculated from PA data as the number of cells with graphene content over the threshold divided by the total number of analyzed cells. Note the logarithmic incubation duration scale. Error bars show counting error calculated as $n^{1/2}$ (n : number of cells) normalized to the total number of cells.

alone. The gray-filled histograms represent the Fluorescence Minus One (FMO) negative staining controls, while the orange-filled histogram represents the receptor expression when JAWSII cells were treated with media alone. The rest of the histograms were not filled in. For example, the green unfilled histogram represents the receptor expression at 2 hours (Fig. 6). Compared to our FMO controls (gray-filled histogram) and media alone (orange-filled histogram), the lipopolysaccharide (LPS)-stimulated positive control (blue histogram), was able to up regulate CD86 and MHC-I (Fig. 6).

Since co-stimulation is essential for DC induction of T cell stimulation, we chose to focus on CD86. The expression

pattern of CD86 was dynamic, as the expression continued to change during $50 \mu\text{g mL}^{-1}$ graphene exposure for both the 24 (red histogram) and 72 hours (purple histogram) time points (Fig. 6). Notably, MHC class-I expression profiles showed relatively similar trends during the 5 and $10 \mu\text{g mL}^{-1}$ graphene treatments compared to the medium alone. However, during the $50 \mu\text{g mL}^{-1}$ graphene treatment, the MHC class I receptor expression decreased over time compared to the medium (purple histogram vs. orange-filled histogram, Fig. 6). The reason for the decrease in MHC class I receptor expression may be due to the decreased inactivation state of the DC. However, this remains to be further investigated. Notably,

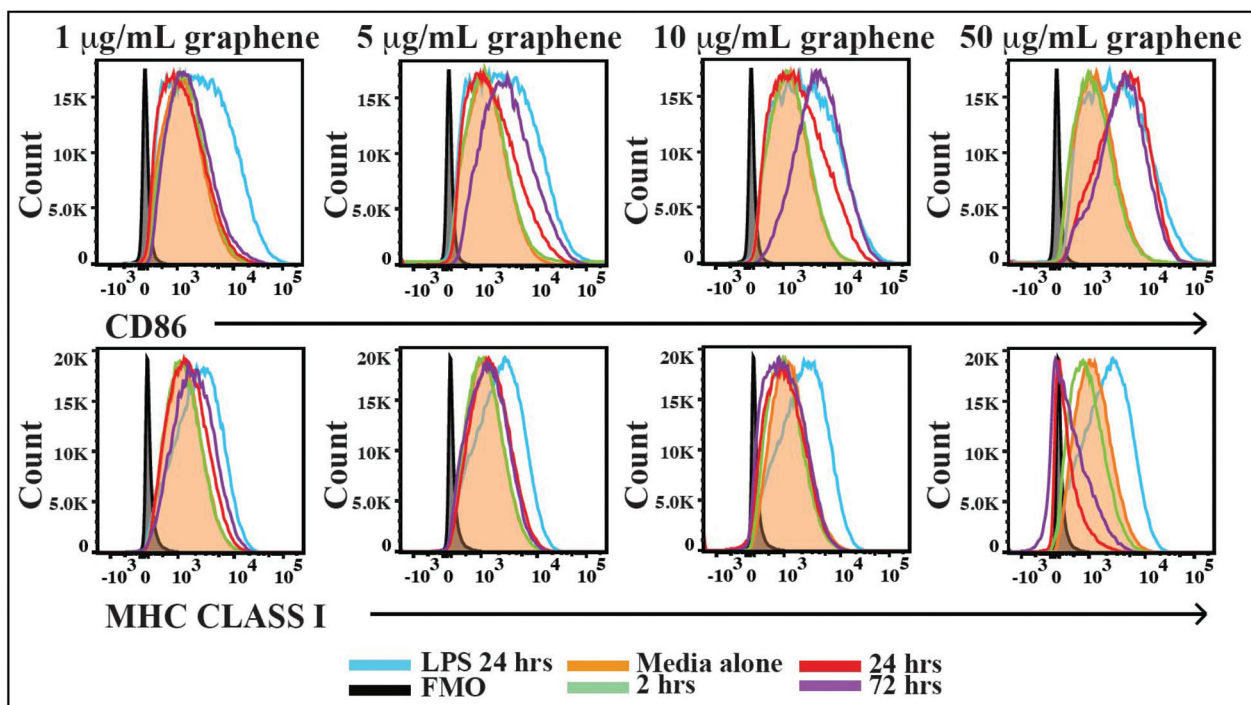


Fig. 6 Dynamic surface receptor expression on JAWSII cells after graphene treatment. JAWSII cells were treated with medium alone (orange-filled histogram), $5 \mu\text{g mL}^{-1}$ LPS (blue histogram) or the following concentrations of graphene: $1 \mu\text{g mL}^{-1}$ (left), $5 \mu\text{g mL}^{-1}$ (left middle), $10 \mu\text{g mL}^{-1}$ (right middle), and $50 \mu\text{g mL}^{-1}$ (right) for 2 hours (light green histogram), 24 hours (red histogram), and 72 hours (purple histogram). Data are representative of two independent experiments; $n = 5$ for the $10 \mu\text{g mL}^{-1}$ graphene-treated JAWSII cells; for all other treatments, $n = 6$.

graphene did not induce discernable apoptosis in JAWSII cells, even at the highest treatment of $50 \mu\text{g mL}^{-1}$, in comparison to the dexamethasone positive controls and our Annexin 5 compensation single stain controls (Fig. S17 and S18†). However, the induction of other surface expression changes was much more dynamic (Fig. S17†). In general, the changes in the expression of CD86 and MHC class I receptors were induced by graphene.

Raman/PAM imaging shows that an average effective dose of graphene of 6.5 pg causes changes in DC cell surface expression (Fig. 4(a), 6 and Fig. S17†). However, it is also crucial to consider effective dose distribution at a single cell level. Our data shows that at high graphene concentration ($50 \mu\text{g mL}^{-1}$), most of the cells (80–100% of JAWSII cells) acquired $>2.5 \text{ pg}$ of graphene. At a lower dose of graphene ($5\text{--}10 \mu\text{g mL}^{-1}$), only 40–80% of the cells acquired that amount and, thus, may undergo nanomaterial-induced changes. The correlation of graphene effective dose with surface expression changes may be crucial for understanding whether changes are dose related or caused by small amounts of the nanomaterial triggering certain molecular pathways.

Overall, the exposure dose of graphene results in dynamic patterns of surface receptor expression profiles, with little apoptosis or necrosis recorded (Fig. S16†). Therefore, graphene induced changes in surface receptor expression at low concentrations, but it did not induce detectable apoptotic events. Though our WST-1 data indicated that some JAWSII cells

underwent apoptosis and necrosis, our Annexin V data indicated that at the same 30 hour time point, at the highest $50 \mu\text{g mL}^{-1}$ treatment with graphene, apoptosis was minimal. In addition, we have observed that graphene could interfere in the WST-1 assays, indicating that higher concentrations of graphene could result in an inaccurate reading. Though apoptosis could potentially have an effect on cell surface expression of these markers, the 30 hour time point Annexin V data indicates that this was not the case, as apoptosis was minimal. The difference in receptor expression is not due to cell viability, as, by the 72 hour time point, CD86 expression increased, while MHC class I expression decreased. Surface cell expression was recapitulated in an $n = 6$ (except for the $10 \mu\text{g mL}^{-1}$ concentration). Though graphene absorption on the surface of the cells could impact antibody binding, we were able to recapitulate receptor expression in our replicates. Thus, the impact of the effective dose on the upregulation of these cell surface markers may indicate that the DCs are poised to become “licensed” as an indicator of the DC potential to initiate an immune response. However, to fully assess graphene induced immune responses, based on the structural (dimensions, shapes, number of layers) and physical-chemical (functionalization, level of oxidation, *etc.*) characteristics, in the future we propose to move beyond DCs by using primary immune cells instead of cell lines. Furthermore, other immune cells lineages (such as T cells, B cells, and NK cells) will have to be assessed. Overall, a more adept way to fully

assess the graphene-induced immune response would have to perform *in vivo* using appropriate murine models. Another major consideration that needs to be further investigated is the possibility that graphene changes the microenvironment of the cells and these processes will result in changes to the receptor expressions of the cells. Graphene is known to present an excellent platform for protein attachment (protein corona), therefore resulting in media with modified characteristics.

The method that we presented in this work has the ability to provide information regarding the amount of graphene that will interact with various cell lines, down to single cell level. This indicates the ability to understand biological phenomena based on the amount of the graphene that actually interacts with the cells, rather than the amount of graphene that is delivered into the cell media. Therefore, this could be of great help to the various scientists in the field. Some of the limitations of this approach include the fact that for each type of graphene (oxidation or functionalization level, dimensional characteristics, *etc.*) new calibration curves might have to be established, which could prove cumbersome. Another aspect is that the method could possibly be extended into *in vivo* graphene analysis/detection in tissues, but other major considerations have to be considered for such applications, and which include laser beam attenuation and/or diameter variation.

Conclusions

In conclusion, we presented a spectroscopy-based approach to assess the amount of graphene in a model biological system, down to the individual cell. We have found that graphene interacted with two cell lines, particularly with JAWSII DCs, in a concentration- and time-dependent manner. However, the cell-to-cell variations were relatively large. This approach can be used to understand the impact that graphene or other nanomaterials can have on cells by correlating the observed biological effects with the amount of nanomaterials that actually interact with the cells. Understanding the impact that the amount of graphene has on immune cells such as DCs may be vital to developing graphene-based drugs for cancer immunotherapy or the treatment of autoimmune diseases. This research is an essential step forward for human risk assessments that determine the concentrations of nanomaterials to which humans can be exposed without major toxicological effects.

Conflicts of interest

The authors declare no conflict of interest

Acknowledgements

We acknowledge financial support from the U.S. Food and Drug Administration award HHSF223201210189C (adminis-

tered through the Arkansas Research Alliance). The views presented in this paper are not necessarily those of the U.S. FDA. Partial funding for this work was also provided by the Center for Advanced Surface Engineering, under the National Science Foundation grant IIA-1457888 and the Arkansas Asset III EPSCoR Program, National Institutes of Health (NIH), grant number 14.Z50.31.0044. We thank Emily Davis for her editorial assistance on this manuscript. "The information in these materials is not a formal dissemination of information by FDA and does not represent agency position or policy".

References

- 1 A. K. Geim, Graphene: Status and Prospects, *Science*, 2009, **324**, 1530–1534.
- 2 A. K. Geim and K. S. Novoselov, The rise of graphene, *Nat. Mater.*, 2007, **6**, 183–191.
- 3 K. S. Novoselov, *et al.*, Electric Field Effect in Atomically Thin Carbon Films, *Science*, 2004, **306**, 666–669.
- 4 A. Das, *et al.*, Monitoring dopants by Raman scattering in an electrochemically top-gated graphene transistor, *Nat. Nanotechnol.*, 2008, **3**, 210–215, DOI: 10.1038/nnano.2008.67.
- 5 E. J. Petersen, D. X. Flores-Cervantes, T. D. Bucheli, L. Elliott, J. A. Fagan, A. Gogos, S. K. Hanna, R. Kaegi, E. Mansfield, A. R. Montoro Bustos, D. L. Plata, V. Reipa, P. K. Westerhoff and M. R. Winchester, Quantification of carbon nanotubes in environmental matrices: Current capabilities, case studies, and future prospects, *Environ. Sci. Technol.*, 2016, **50**, 4587–4605.
- 6 K. Doudrick, T. Nosaka, P. Herckes and P. Westerhoff, Quantification of graphene and graphene oxide in complex organic matrices, *Environ. Sci.: Nano*, 2015, **2**, 60–67, DOI: 10.1039/C4EN00134F.
- 7 Z. A. Nima, *et al.*, Single-walled carbon nanotubes as specific targeting and Raman spectroscopic agents for detection and discrimination of single human breast cancer cells, *J. Biomed. Opt.*, 2013, **18**, 055003–055003, DOI: 10.1117/1.jbo.18.5.055003.
- 8 L. M. Malard, M. A. Pimenta, G. Dresselhaus and M. S. Dresselhaus, Raman spectroscopy in graphene, *Phys. Rep.*, 2009, **473**, 51–87, DOI: 10.1016/j.physrep.2009.02.003.
- 9 S. Pérez, M. L. Farré and D. Barceló, Analysis, behavior and ecotoxicity of carbon-based nanomaterials in the aquatic environment, *TrAC, Trends Anal. Chem.*, 2009, **28**, 820–832, DOI: 10.1016/j.trac.2009.04.001.
- 10 D. R. Johnson, M. M. Methner, A. J. Kennedy and J. A. Steevens, Potential for Occupational Exposure to Engineered Carbon-Based Nanomaterials in Environmental Laboratory Studies, *Environ. Health Perspect.*, 2010, **118**, 49–54.
- 11 K.-H. Liao, Y.-S. Lin, C. W. Macosko and C. L. Haynes, Cytotoxicity of Graphene Oxide and Graphene in Human Erythrocytes and Skin Fibroblasts, *ACS Appl. Mater. Interfaces*, 2011, **3**, 2607–2615, DOI: 10.1021/am200428v.

- 12 O. Akhavan, E. Ghaderi and A. Akhavan, Size-dependent genotoxicity of graphene nanoplatelets in human stem cells, *Biomaterials*, 2012, **33**, 8017–8025, DOI: 10.1016/j.biomaterials.2012.07.040.
- 13 K. A. Wang, A. M. Rao, P. C. Eklund, M. S. Dresselhaus and G. Dresselhaus, Observation of higher-order infrared modes in solid C₆₀ films, *Phys. Rev. B: Condens. Matter Mater. Phys.*, 1993, **48**, 11375–11380.
- 14 W. Majeed, S. Bourdo, D. M. Petibone, V. Saini, K. B. Vang, Z. A. Nima, K. M. Alghazali, E. Darrigues, A. Ghosh, F. Watanabe, D. Casciano, S. F. Ali and A. S. Biris, The role of surface chemistry in the cytotoxicity profile of graphene, *J. Appl. Toxicol.*, 2016, **37**, 462–470.
- 15 D. A. Nedosekin, J. Nolan, C. Cai, S. E. Bourdo, Z. Nima, A. S. Biris and V. P. Zharov, In vivo noninvasive analysis of graphene nanomaterial pharmacokinetics using photoacoustic flow cytometry, *J. Appl. Toxicol.*, 2017, **37**, 1297–1304.
- 16 S. Böhme, *et al.*, Quantification of Al₂O₃ nanoparticles in human cell lines applying inductively coupled plasma mass spectrometry (neb-ICP-MS, LA-ICP-MS) and flow cytometry-based methods, *J. Nanopart. Res.*, 2014, **16**, 2592, DOI: 10.1007/s11051-014-2592-y.
- 17 J. S. Becker, *et al.*, Bioimaging of metals by laser ablation inductively coupled plasma mass spectrometry (LA-ICP-MS), *Mass Spectrom. Rev.*, 2010, **29**, 156–175, DOI: 10.1002/mas.20239.
- 18 C. Austin, D. Hare, T. Rawling, A. M. McDonagh and P. Doble, Quantification method for elemental bioimaging by LA-ICP-MS using metal spiked PMMA films, *J. Anal. At. Spectrom.*, 2010, **25**, 722–725, DOI: 10.1039/B911316A.
- 19 F. G. P. Bogdan, *et al.*, Mapping metals in Parkinson's and normal brain using rapid-scanning X-ray fluorescence, *Phys. Med. Biol.*, 2009, **54**, 651.
- 20 B. D. Holt, K. N. Dahl and M. F. Islam, Quantification of Uptake and Localization of Bovine Serum Albumin-Stabilized Single-Wall Carbon Nanotubes in Different Human Cell Types, *Small*, 2011, **7**, 2348–2355, DOI: 10.1002/smll.201100437.
- 21 D. A. Nedosekin, M. Sarimollaoglu, E. V. Shashkov, E. I. Galanzha and V. P. Zharov, Ultra-fast photoacoustic flow cytometry with a 0.5 MHz pulse repetition rate nanosecond laser, *Opt. Express*, 2010, **18**, 8605–8620, DOI: 10.1364/OE.18.008605.
- 22 V. Ntziachristos, Going deeper than microscopy: the optical imaging frontier in biology, *Nat. Methods*, 2010, **7**, 603–614.
- 23 W. R. Hendee and E. R. Ritenour, *Medical Imaging Physics*, John Wiley & Sons, Inc., 2002, pp. 303–316.
- 24 D. A. Nedosekin, *et al.*, In vivo noninvasive analysis of graphene nanomaterial pharmacokinetics using photoacoustic flow cytometry, *J. Appl. Toxicol.*, 2017, **37**, 1297–1304, DOI: 10.1002/jat.3467.
- 25 F. Bonaccorso, Z. Sun, T. Hasan and A. C. Ferrari, Graphene photonics and optoelectronics, *Nat. Photonics*, 2010, **4**, 611–622.
- 26 S. Chen, *et al.*, Mass spectrometry imaging reveals the sub-organ distribution of carbon nanomaterials, *Nat. Nanotechnol.*, 2015, **10**, 176–182, DOI: 10.1038/nnano.2014.282.
- 27 R. M. Steinman, The Dendritic Cell System and its Role in Immunogenicity, *Annu. Rev. Immunol.*, 1991, **9**, 271–296, DOI: 10.1146/annurev.iy.09.040191.001415.
- 28 R. M. Steinman and J. W. Young, Signals arising from antigen-presenting cells, *Curr. Opin. Immunol.*, 1991, **3**, 361–372, DOI: 10.1016/0952-7915(91)90039-4.
- 29 C.-A. Dutertre, L.-F. Wang and F. Ginhoux, Aligning bona fide dendritic cell populations across species, *Cell. Immunol.*, 2014, **291**, 3–10, DOI: 10.1016/j.cellimm.2014.08.006.
- 30 J. K. H. Tan and H. C. O'Neill, Maturation requirements for dendritic cells in T cell stimulation leading to tolerance versus immunity, *J. Leukocyte Biol.*, 2005, **78**, 319–324.
- 31 J. Xiaozhou, S. Caixia, R.-L. Jose, Y. Hong and R. C. Brunham, Characterization of Murine Dendritic Cell Line JAWS II and Primary Bone Marrow-Derived Dendritic Cells in Chlamydia muridarum Antigen Presentation and Induction of Protective Immunity, *Infect. Immun.*, 2007, **76**, 2392–2401.
- 32 L. Zapala, *et al.*, Optimization of activation requirements of immature mouse dendritic JAWSII cells for in vivo application, *Oncol. Rep.*, 2011, **25** 3, 831–840.
- 33 G. Sauerbrey, Verwendung von Schwingquarzen zur Wägung dünner Schichten und zur Mikrowägung, *Z. Phys.*, 1959, **155**, 206–222, DOI: 10.1007/BF01337937.
- 34 E. Koutsoumpeli, *et al.*, Antibody Mimetics for the Detection of Small Organic Compounds Using a Quartz Crystal Microbalance, *Anal. Chem.*, 2017, **89**, 3051–3058, DOI: 10.1021/acs.analchem.6b04790.
- 35 W.-L. Kao, H.-Y. Chang, K.-Y. Lin, Y.-W. Lee and J.-J. Shyue, Effect of Surface Potential on the Adhesion Behavior of NIH3T3 Cells Revealed by Quartz Crystal Microbalance with Dissipation Monitoring (QCM-D), *J. Phys. Chem. C*, 2017, **121**, 533–541, DOI: 10.1021/acs.jpcc.6b11217.
- 36 Y. Wang and M. A. Moss, Effect of Resveratrol and Derivatives on Interactions between Alzheimer's Disease Associated A β ; Protein Oligomers and Lipid Membranes: A Quartz Crystal Microbalance Analysis, *Biophys. J.*, 2016, **110**, 256a, DOI: 10.1016/j.bpj.2015.11.1405.
- 37 T. Zhou, K. A. Marx, M. Warren, H. Schulze and S. J. Braunhut, The Quartz Crystal Microbalance as a Continuous Monitoring Tool for the Study of Endothelial Cell Surface Attachment and Growth, *Biotechnol. Prog.*, 2000, **16**, 268–277, DOI: 10.1021/bp000003f.
- 38 N.-J. Cho, C. W. Frank, B. Kasemo and F. Hook, Quartz crystal microbalance with dissipation monitoring of supported lipid bilayers on various substrates, *Nat. Protocols*, 2010, **5**, 1096–1106.
- 39 J. Xi, J. Y. Chen, M. P. Garcia and L. S. Penn, Quartz Crystal Microbalance in Cell Biology Studies, *J. Biochips Tissue Chips*, 2013, **S5**, 001.

- 40 A. R. Biris, *et al.*, Synthesis of tunable core-shell nanostructures based on TiO₂-graphene architectures and their application in the photodegradation of rhodamine dyes, *Phys. E*, 2016, **81**, 326–333, DOI: 10.1016/j.physe.2016.03.028.
- 41 L. G. Cançado, *et al.*, General equation for the determination of the crystallite size L_a of nanographite by Raman spectroscopy, *Appl. Phys. Lett.*, 2006, **88**, 163106, DOI: 10.1063/1.2196057.
- 42 T. Deckert-Gaudig and V. Deckert, Tip-enhanced Raman scattering (TERS) and high-resolution bio nano-analysis—a comparison, *Phys. Chem. Chem. Phys.*, 2010, **12**, 12040–12049, DOI: 10.1039/C003316B.
- 43 A. Danielli, *et al.*, Label-free photoacoustic nanoscopy, *J. Biomed. Opt.*, 2014, **19**, 086006–086006, DOI: 10.1117/1.JBO.19.8.086006.
- 44 D. A. Nedosekin, E. I. Galanzha, E. Dervishi, A. S. Biris and V. P. Zharov, Super-Resolution Nonlinear Photothermal Microscopy, *Small*, 2013, **10**, 135–142, DOI: 10.1002/smll.201300024.
- 45 J.-H. Liu, *et al.*, Effect of size and dose on the biodistribution of graphene oxide in mice, *Nanomedicine*, 2012, **7**, 1801–1812, DOI: 10.2217/nnm.12.60.
- 46 O. Akhavan, E. Ghaderi, E. Hashemi and E. Akbari, Dose-dependent effects of nanoscale graphene oxide on reproduction capability of mammals, *Carbon*, 2015, **95**, 309–317, DOI: 10.1016/j.carbon.2015.08.017.
- 47 C. Cai, *et al.*, In vivo photoacoustic flow cytometry for early malaria diagnosis, *Cytometry, Part A*, 2016, **89**, 531–542, DOI: 10.1002/cyto.a.22854.
- 48 J. L. Cocchiario, Y. Kumar, E. R. Fischer, T. Hackstadt and R. H. Valdivia, Cytoplasmic lipid droplets are translocated into the lumen of the *Chlamydia trachomatis* parasitophorous vacuole, *Proc. Natl. Acad. Sci.*, 2008, **105**, 9379.